CHAPTER-2

Lead halide perovskite-nickel(II) complex improves visible light photoredox C–N coupling

2.1. Introduction

Amides, essential in peptides, polymers, agrochemicals,[1-10] and pharmaceuticals,[11-15] are traditionally synthesized under harsh conditions with limited substrate scope and generating significant waste.[16-32] To address these challenges, photocatalytic methods have emerged, though many homogeneous approaches rely on expensive catalysts, non-oxygen oxidants, and show poor tolerance toward secondary amines. Simpler systems using phenazine salts, Rose Bengal, and aminoanthraquinone derivatives have shown promise.[26] Heterogeneous catalysts like Ag/g-C_3N_4, Ni/g-C_3N_4, Ag_2O/P–C_3N_4, TiO_2, and Fe_3O_4/PDA/CdS have also been developed for aldehyde oxidative amination.[26] Photocatalytic amide synthesis via aldehyde–amine coupling using quantum dots as the photocatalyst has gained huge attention because of its robustness and tolerance to versatile substrates having electron-donating, withdrawing, and sterically bulky groups.[26,27]

This study explored the photoredox activity of $CsPbBr_3$ QDs to synthesize structurally diverse amides via aldehyde–amine coupling. To enhance charge transfer, catalytic site accessibility, and selectivity, [Ni(dmgH)$_2$] was introduced as a cocatalyst. Recently, Nickel offers diverse reactivity and replaces costly Pd, enabling novel mechanisms. Nickel metallaphotoredox catalysis has recently expanded traditional Ni catalysis, allowing efficient C–C and carbon-heteroatom (C–X) bond formation. Yet, most dual Ni/photoredox systems still depend on carefully chosen metal complexes for the activation of substrates. Molander's group notably advanced single-electron transmetalation, now central to this field.

In this study, the [Ni(dmgH)$_2$]–$CsPbBr_3$ photoredox system achieved high efficiency in oxidative C–N bond formation with secondary amines, reaching yields of amides up to 92%. The catalyst demonstrated good recyclability, retaining activity over four cycles. Transient

absorption spectroscopy further confirmed that [$Ni(dmgH)_2$] acts as an electron funnel, promoting rapid electron transfer from the QDs to the catalytic sites.

2.2. Chemicals

Lead bromide (99.9%), copper bromide (99.9%), cesium bromide, oleic acid (OA, 90%), 1-octadecene (ODE, 91%), 2,3-butanedione monoxime, dimethyl sulfoxide (DMSO), titanium butoxide, sodium tungstate dihydrate, propane-2-ol, and tetrabutylammonium hexafluorophosphate ($TBHPF_6$) were purchased from Sigma-Aldrich. Nickel chloride hexahydrate was purchased from SD Fine-Chemical Limited. Ethyl acetate (99.9%), sodium hydroxide, dimethylglyoxime ($dmgH_2$), cesium carbonate (99.9%), oleylamine (OAm, 90%), sodium hydroxide, and anhydrous solvents like tetrahydrofuran, toluene, and acetonitrile were purchased from Sisco Research Laboratories Pvt. Ltd, India. 2,3-Diaminonapthalene and 9,10-diphenylanthracene were purchased from BLD Pharmatech (India) Private Limited. *P*-Nitro-Blue tetrazolium chloride (NBT) and *o*-Tolidine were purchased from Sigma-Aldrich. Cobalt chloride hexahydrate, Bismuth nitrate pentahydrate, potassium bromide ethylenediamine, Chloroform-d ($CDCl_3$), hexane, and silica gel were purchased from Merck. All aldehydes, alcohols, amines, and other organic substrates were purchased from either Sigma-Aldrich, SRL, or Merck and BLD Pharmatech (India) Private Limited.

2.3. Instruments

The PXRD data were acquired within 2θ range of 5-80° using a Rigaku D/MAX RINT-2000 X-Ray diffractometer, with Cu-K_α (λ = 1.5418Å) radiation.

The X-ray photoelectron spectroscopy (XPS) was conducted on a VG/VG ESCA LAB 220i X-ray photoelectron spectrometer. The acquired XPS was deconvoluted and analyzed using Origin 8.5 software. Diffuse reflectance spectroscopy (DRS) measurements using UV-

Vis were conducted utilizing an AvaSpec-ULS2048L instrument. Photoluminescence spectra were recorded on a TCSPC system from Horiba Yovin (Delta Flex).

The detection of reactive oxygen species (ROS) and H_2O_2 was performed using the UV-Vis spectra of the complexes, recorded with an Agilent Cary 60 UV-Vis spectrophotometer.

Transmission electron microscopy (TEM) analyses were conducted using an FEI Tecnai G2 20 S-TWIN instrument equipped with an energy-dispersive X-ray spectrometer (EDAX, r-TEM SUTW). For TEM mapping analysis, the JEOL JEM-2100 instrument was used and operated at 120 kV accelerating voltage.

^{1}H-NMR and ^{13}C-NMR spectra were recorded on an AVH D 500 AVANCE III HD 500 MHz One Bay NMR Spectrometer from Bruker Bio Spin International and Advance Neo 600 MHz Bruker India Scientific. The chemical shifts and coupling constants were reported in ppm. The abbreviations used are as follows: "s" for singlet, "bs" for broad singlet, "d" for doublet, "t" for triplet, and "m" for multiple. Residual solvent signals ($CDCl_3$: δ_H = 7.28-7.29 ppm and δ_C = 77.01-77.16 ppm) were used as the references for ^{1}H and ^{13}C NMR spectra, respectively.

HR-MS (m/z) were recorded on a SCIEX X500R QTOF in electron ionization or electrospray ionization (ESI) mode.

Electron paramagnetic resonance (EPR) studies were performed at room temperature using Bruker A300-9.5/12/S/W.

Light source for the photocatalytic reaction: (JACKAL, LED 3 Watt blue light, 460 ± 3 nm). 5 Lights were used together.

Ultrafast transient absorption

The ultrafast Transient Absorption (TA) experimental arrangement utilized an 80 MHz mode-locked laser. The samples were kept in a sealed quartz cuvette with a path length of 2 mm. The

samples used in the experiments were suspended in THF, and the OD was maintained ~0.4 in 2 mm path length. The sample was stirred using a magnetic stirrer. The pump wavelength of 370 nm (10 nJ) was generated from Opera solo OPA. A White light probe was generated by focusing a segment of the amplified output centered at 800 nm by an Astrella amplifier from Coherent USA operating at 1 kHz on a CaF_2 Crystal. The white light was split using a beam splitter to generate both signal and reference beams. These beams were directed through a fiber coupling unit to the detector (photodiode detector array) to capture the pump-induced changes at various delay times of the probe beam. All spectra were chirp-corrected, and the measurements were performed within a delay time window of up to 6 ns. The TA spectra are analyzed using Surface Explorer, V.4.2 software.

2.4. Experimental

2.4.1. Synthesis of $CsPbBr_3$ QDs

$CsPbBr_3$ QDs were prepared using a modified version of a previously reported method.[33] Initially, Cs_2CO_3 (130.3 mg, 0.4 mmol), OA (0.5 mL), and ODE (6 mL) were added to a 250 mL three-neck round-bottom flask. The mixture was heated at 120 °C under a nitrogen atmosphere for 1 hour, followed by heating at 150 °C for 10 minutes until the Cs_2CO_3 completely dissolved, forming a clear Cs-oleate solution. This precursor was maintained at 100 °C for later use.

Separately, $PbBr_2$ (73 mg, 0.2 mmol) and ODE (10 mL) were placed in another three-neck flask and degassed under vacuum at 120 °C for 1 hour. The atmosphere was then switched to nitrogen, and dried OA and OAm, 0.5 mL each, were introduced. The mixture was heated to 170 °C to fully dissolve the $PbBr_2$. Once the solution was clear, 0.4 mL of the pre-heated Cs-oleate solution was swiftly injected, and the mixture was stirred for approximately 5 seconds.

The reaction was then rapidly quenched by placing the flask in an ice-water bath. The resulting product was purified by centrifugation at varying speeds (6000–14000 rpm) and washed with ethyl acetate. Finally, the yellow $CsPbBr_3$ precipitate was collected and dried under vacuum.

2.4.2. Synthesis of Nickel(II) dimethylglyoxime complex

$Ni(dmgH)_2$ was synthesized following a modified version of a reported method.[38] A solution of dimethylglyoxime (2.2 mmol) in 20 mL ethanol was slowly added to an aqueous solution of $NiCl_2.6H_2O$ (1 mmol). The pH of the mixture was adjusted to around 9 using aqueous ammonia to create an alkaline environment. After stirring the reaction mixture for 15 minutes, the resulting solid was collected by filtration and washed thoroughly with ethanol and deionized water. The obtained solid was then dried at 60 °C for 12 hours.

Additionally, salen ligands were prepared based on established literature procedures.[3,4] The Ni(II)–salen complex was also synthesized using a previously reported method.[5]

2.4.3. Preparation of [Ni]-$CsPbBr_3$

93 mg $CsPbBr_3$ QDs were dispersed in 7 mL of tetrahydrofuran (THF). Separately, 7 mg of $Ni(dmgH)_2$ was dissolved in 3 mL of THF and then added to the $CsPbBr_3$ dispersion. The resulting mixture was stirred in the dark for 10 minutes to form a uniform suspension, referred to as 7% [Ni]-$CsPbBr_3$. For each reaction, 1 mL of this catalyst solution was used. For solid-state characterization, 7% [Ni]-$CsPbBr_3$ sample was obtained by removing the solvent under vacuum. Similarly, different wt.% of cocatalysts were loaded as listed in **Table 2.1.**

Table 2.1. Description of the catalyst.

S.N.	Photocatalyst	Cocatalyst	Loading (wt.%)	Code
1	$CsPbBr_3$	$Ni(dmgH)_2$	0	$CsPbBr_3$
2	$CsPbBr_3$	$Ni(dmgH)_2$	3	3% [Ni]-$CsPbBr_3$
3	$CsPbBr_3$	$Ni(dmgH)_2$	5	5% [Ni]-$CsPbBr_3$
4	$CsPbBr_3$	$Ni(dmgH)_2$	7	7% [Ni]-$CsPbBr_3$
5	$CsPbBr_3$	$Ni(dmgH)_2$	9	9% [Ni]-$CsPbBr_3$

2.5. Photocatalytic activity test

The C–N coupling reaction between the aldehyde and amine was performed in a 15 mL quartz vial connected to a water circulation system. A mixture of aldehyde (0.5 mmol) and amine (1 mmol) was prepared in 2 mL of THF. To this solution, 1.0 mL of a photocatalyst solution in THF (containing 10 mg of photocatalyst) was added. The reaction mixture was stirred in the dark for 10 minutes to achieve a suspension and to establish adsorption-desorption equilibrium between the catalyst and substrates. The vial was positioned 8 cm from the light source and irradiated for 18 hours under stirring (400 rpm). The temperature was maintained at 35 ± 3 °C throughout the reaction. After completion, the reaction mixture was centrifuged at 15,000 rpm for 10 minutes to separate the photocatalyst. The liquid phase was collected and subjected to work-up, and the isolated product yield was reported. The product was characterized by ^{1}H and ^{13}C NMR spectroscopy. After each amination reaction, the photocatalyst was washed several times with ethanol, recovered by centrifugation, and vacuum-dried overnight for reuse in recycling tests.

2.6. Working electrode preparation and photoelectrochemical measurements

Photoelectrochemical measurements, photocurrent response, electrochemical impedance spectroscopy (EIS), and Mott-Schottky analysis were performed on Metrohm Auto Lab M204 workstation under either 15 W blue LED or 100 W visible light illumination. A conventional three-electrode setup was employed, comprising a platinum wire as the counter electrode, an Ag/AgCl electrode as the reference, and a working electrode made of fluorine-doped tin oxide (FTO) glass loaded with 3 mg of catalyst. The electrolyte consisted of 0.1 M tetrabutylammonium hexafluorophosphate ($TBAPF_6$) dissolved in ethyl acetate. The FTO glass was initially cleaned by ultrasonication in ethanol and acetone, followed by rinsing with

deionized water and isopropyl alcohol (IPA). Subsequently, 3 mg of catalyst was dispersed in 1 mL of toluene, 50 µL of 0.5 wt.% Nafion solution and sonicated for 10 minutes. A 500 µL suspension was then dropped onto a 1 cm^2 area of FTO and allowed to dry (room temperature) for about 50 minutes under ambient conditions.

2.7. Results and discussion

2.7.1. Characterizations of the catalysts

Metal halide perovskite $CsPbBr_3$ QDs were synthesized via the hot-injection method following a reported procedure (**Experimental section 2.4.1**).[33] Powder X-ray diffraction (PXRD) confirmed their monoclinic crystal structure (JCPDS card no. 18-0364) (**Figure 2.1a-b**).[33,34] Transmission electron microscopy (TEM) showed an average particle size of 5.5 ± 1 nm (**Figure 2.1c**), and HRTEM identified lattice spacings corresponding to the (200), (210), (202), (211), and (002) planes (**Figure 2.1c-e**).[35,36] Energy-dispersive X-ray (EDX) spectroscopy confirmed the presence of Cs, Pb, and Br (**Figure 2.1f**).

2.7.2 Optoelectronic properties of catalysts

For the photoredox reactions, $Ni(dmgH)_2$ was employed as a cocatalyst to enhance efficiency and selectivity. Varying the $Ni(dmgH)_2$ content (3, 5, 7, and 9 wt%) led to notable differences in photocatalytic activity (**Table 2.1**) (discussed later). Thus, we conducted detailed optoelectronic characterization of the catalyst systems. UV-visible diffuse reflectance spectroscopy (DRS) showed a bandgap of 2.28 eV for $CsPbBr_3$, which remained unchanged upon $Ni(dmgH)_2$ addition (**Figure 2.2a-b**).[37] However, a broad ligand-to-metal charge transfer (LMCT) band from $Ni(dmgH)_2$ appeared after incorporation (**Figure 2.2a**),[38] and blue shift in the absorption maximum indicated electronic interaction between $Ni(dmgH)_2$ and $CsPbBr_3$. In Mott–Schottky (MS) plots, both $CsPbBr_3$ QDs and $Ni(dmgH)_2$ showed positive slopes between

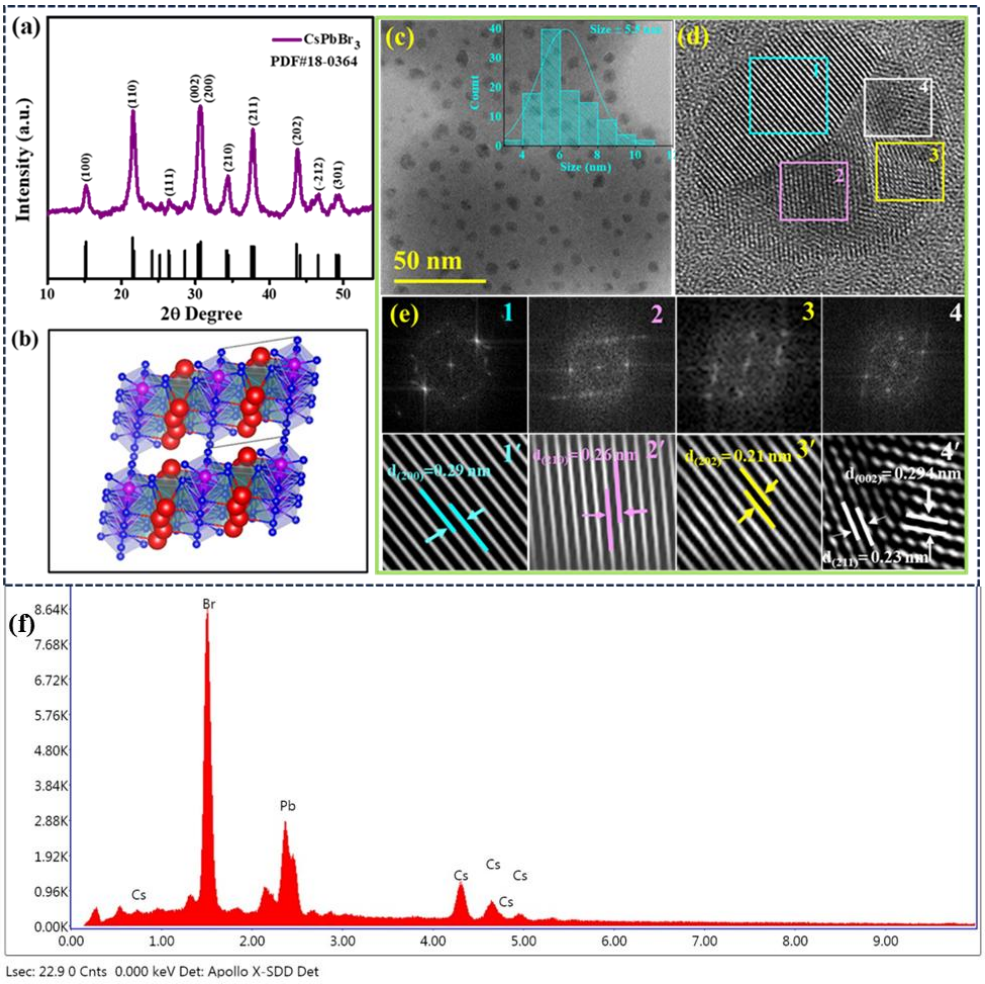

Figure 2.1. (a) PXRD pattern of monoclinic $CsPbBr_3$ QDs. (b) Crystal structure of monoclinic $CsPbBr_3$ QDs. (c) TEM image of $CsPbBr_3$ QDs with inset showing size distribution. (d) High-resolution TEM image highlighting crystal planes of monoclinic $CsPbBr_3$ QDs. (e) FFT (1–4) and corresponding inverse FFT (1′–4′) images from the selected area in (d). (f) EDX spectrum confirming the presence of Cs, Pb, and Br elements.

0.5–1.5 kHz, indicating the formation of an n–n-type heterojunction. Based on the MS data, the flat band potentials were determined to be −0.99 eV for $CsPbBr_3$ and −0.59 eV for $Ni(dmgH)_2$ vs NHE (**Figure 2.2c-d**).[38,39] Considering the conduction band minimum (CBM) of an n-type semiconductor lies about 0.1–0.2 eV above the flat band potential, the CBMs were estimated at −1.09 eV and −0.69 eV, respectively. The valence band maximum (VBM) of

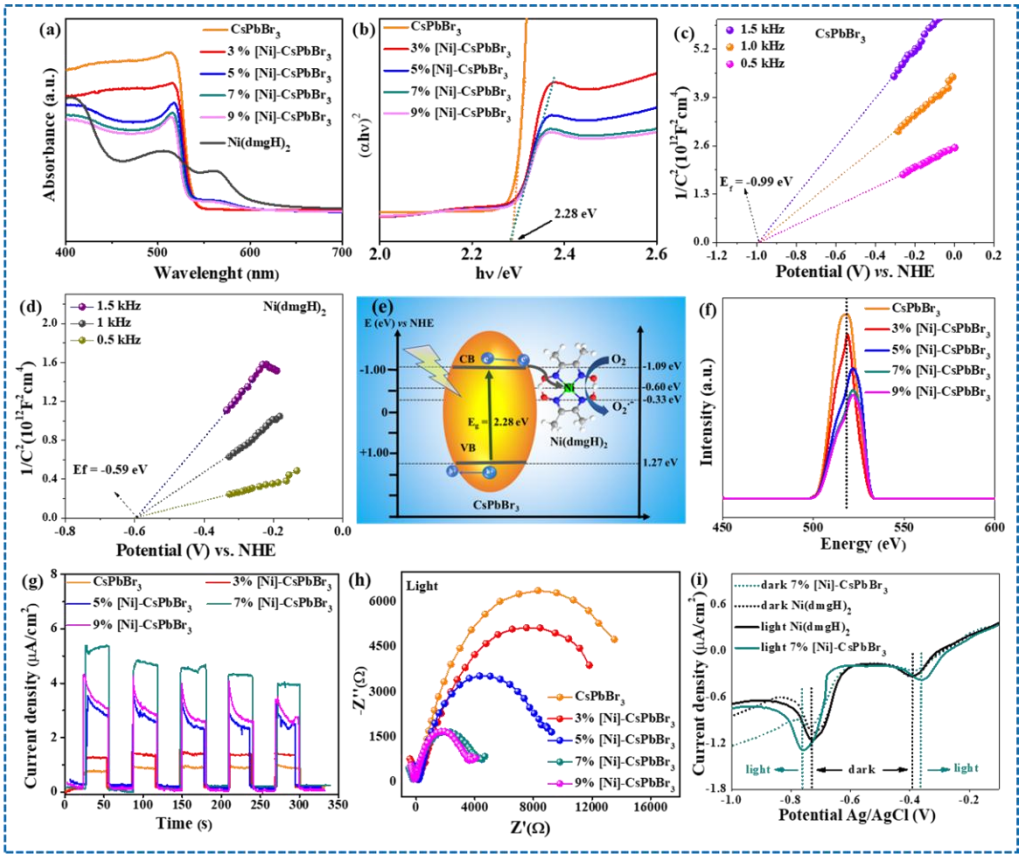

Figure 2.2. (a) UV-vis diffuse reflectance spectra of $CsPbBr_3$ QDs, various wt.% [Ni]-$CsPbBr_3$, and $Ni(dmgH)_2$. (b) Corresponding Tauc plot showing no significant bandgap change upon cocatalyst loading. (c, d) Mott–Schottky plots of $CsPbBr_3$ QDs and $Ni(dmgH)_2$. (e) Energy band positions (CB and VB) derived from Tauc and Mott–Schottky analysis. (f) PL spectra showing reduced charge recombination in [Ni]-$CsPbBr_3$. (g) Photocurrent responses of $CsPbBr_3$ and [Ni]-$CsPbBr_3$ under light/dark conditions. (h) EIS reveals the lowest charge transfer resistance for 7% [Ni]-$CsPbBr_3$. (i) Differential pulse voltammograms (DPV) of $CsPbBr_3$ and 7% [Ni]-$CsPbBr_3$ under dark and light.

Conditions: Electrolyte: 0.1 M $TBAPF_6$ in ethyl acetate (20 mL); electrodes: FTO@photocatalysts (working), Ag/AgCl (reference), Pt wire (counter); 0.0 V vs. Ag/AgCl; light source: 15 W blue LED.

$CsPbBr_3$ was calculated as 1.19 eV vs NHE. Thus, the high Fermi level (E_f) of $CsPbBr_3$ enables efficient electron transfer from its CB to the LUMO of $Ni(dmgH)_2$ (**Figure 2.2e**).[41]

The photoluminescence (PL) spectrum of $CsPbBr_3$ QDs showed an emission peak at 517 nm (**Figure 2.2f**).[42] Introducing $Ni(dmgH)_2$ progressively quenched the PL intensity, indicating suppressed charge recombination (**Figure 2.2f**). This quenching arises from efficient electron

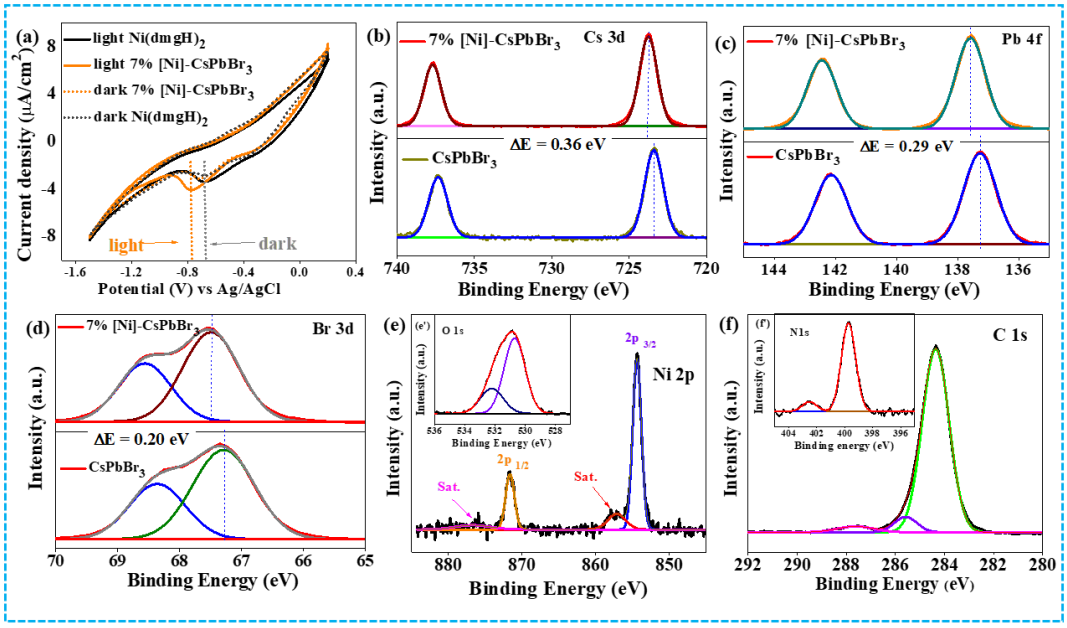

Figure 2.3. (a) Cyclic voltammograms of pristine $CsPbBr_3$ QDs and 7 wt.% [Ni]-$CsPbBr_3$ under dark and light conditions. High-resolution XPS spectra of $CsPbBr_3$ and 7 wt.% [Ni]-$CsPbBr_3$: (b) Cs 3d, (c) Pb 4f, (d) Br 3d. (e) Ni 2p spectrum of 7 wt.% [Ni]-$CsPbBr_3$ confirming the presence of Ni^{2+} species; inset (e′) shows O 1s spectrum indicating adsorbed water (530.71 eV) and –OH groups from the $Ni(dmgH)_2$ ligand (532.23 eV). (f) C 1s spectrum displaying peaks corresponding to C=O (287.64 eV), C=C (285.59 eV), and adventitious carbon (284.37 eV); inset (f′) shows N 1s spectrum with peaks attributed to C=N (399.7 eV) and N–O (402.34 eV) species.

transfer, facilitated by the strong π-acceptor character of the $Ni(dmgH)_2$ ligand backbone.[43] The PL intensity trend correlated with photocatalytic performance, with the highest C–N coupling activity observed for 7% [Ni]-$CsPbBr_3$ (**Table 2.2**). For a more comprehensive understanding, we also recorded the UV spectrum of $Ni(dmgH)_2$ (**Figure 2.2a**), which showed emission peaks at 507 nm and 562 nm.[38] In the 7% [Ni]-$CsPbBr_3$ system, slight shifts in peaks indicated charge transfer from $CsPbBr_3$ QDs to the cocatalyst (**Figure 2.2f**).

Photocurrent measurements under light on/off cycling (**Figure 2.2g**) revealed that [Ni]-$CsPbBr_3$ catalysts exhibited significantly higher photocurrent densities compared to $CsPbBr_3$ QDs alone, with the 7% [Ni]-$CsPbBr_3$ system showing the best response, confirming enhanced

charge separation. $Ni(dmgH)_2$ effectively captures photogenerated electrons from $CsPbBr_3$, reducing charge recombination and promoting charge transfer.[42] Electrochemical impedance spectroscopy (EIS) further supported this, as the Nyquist plots showed smaller arc diameters for [Ni]-$CsPbBr_3$, with 7% [Ni]-$CsPbBr_3$ displaying the lowest charge-transfer resistance (Rct) (**Figure 2.2h**).[44]

The HOMO–LUMO energy gap of the cocatalyst was determined by differential pulse voltammetry (DPV) and cyclic voltammetry (CV) under both light and dark conditions (**Figure 2.2i and Figure 2.3a**). In the ground state, the energy gap between the CB of $CsPbBr_3$ QDs and the LUMO of $Ni(dmgH)_2$ is relatively large. We observed that upon light irradiation, the HOMO of $Ni(dmgH)_2$ shifts to a more positive potential while the LUMO shifts to a more negative potential. This modulation promotes electron transfer from the CB of $CsPbBr_3$ to the LUMO of $Ni(dmgH)_2$, thereby accelerating O_2 reduction to superoxide and enhancing the rate of the photocatalytic C–N coupling reaction.

X-ray photoelectron spectroscopy (XPS) analysis revealed strong electronic interactions between $CsPbBr_3$ QDs and the $Ni(dmgH)_2$ cocatalyst (**Figure 2.3)**. Upon incorporating $Ni(dmgH)_2$, the Cs $3d_{5/2}$ and Cs $3d_{3/2}$ peaks in $CsPbBr_3$ shifted positively by 0.33 eV, indicating electron transfer from the photocatalyst's conduction band to the cocatalyst (**Figure 2.3b)**. Similar positive shifts were observed in the Pb 4f and Br 3d spectra (**Figure 2.3c-d**). Conversely, the Ni $2p_{3/2}$ and $2p_{1/2}$ peaks in 7% [Ni]-$CsPbBr_3$ exhibited negative shifts compared to pure $Ni(dmgH)_2$, suggesting electron accumulation in the cocatalyst's LUMO (**Figure 2.3e-f**). The C 1s, N 1s, and O 1s XPS spectra of 7% [Ni]-$CsPbBr_3$ are presented in (**Figure 2.3e'-f-f'**). Consequently, these findings provide strong evidence of electron transfer from $CsPbBr_3$ QDs to $Ni(dmgH)_2$. These findings confirm efficient electron transfer from

$CsPbBr_3$ QDs to $Ni(dmgH)_2$, enhancing charge separation and photocatalytic activity.

2.7.3. Role of cocatalyst on photoredox activity

The optimization of the photoredox C–N coupling reaction was conducted using 4-nitrobenzaldehyde (1) and piperidine (2) as model substrates (**Table 2.2**). $CsPbBr_3$ QDs alone produced amides with a reduced yield. However, integrating $Ni(dmgH)_2$ with $CsPbBr_3$ QDs significantly enhanced photocatalytic activity (**Table 2.2**). A series of Ni(II)-complexes and salts, including $Ni(dmgH)_2$, $Ni(salen)_2$, $Ni(acac)_2$, and $Ni(OAc)_2{\cdot}4H_2O$, were tested as cocatalysts with $CsPbBr_3$ QDs. Among these, $Ni(dmgH)_2$ was the most effective for the C–N coupling reaction. The cocatalyst amount also strongly influenced photocatalytic activity, with increasing $Ni(dmgH)_2$ concentration leading to higher yields. The optimal yield was achieved with 7% [Ni]-$CsPbBr_3$, and further increases in $Ni(dmgH)_2$ reduced the yield (**Table 2.2**).

The findings from the above investigations highlight the essential role of a cocatalyst in enhancing photocatalytic performance. An ideal cocatalyst should possess an appropriate reduction potential and facilitate efficient separation and transfer of photogenerated charge carriers in $CsPbBr_3$. Specifically, the cocatalyst must efficiently accept electrons from the CB of $CsPbBr_3$ and mediate their transfer to O_2 present in air, leading to the generation of $O_2^{\bullet -}$. While $CsPbBr_3$ activates O_2 to form $O_2^{\bullet -}$, adding $Ni(dmgH)_2$ enhances this via better energy alignment and redox potential, boosting overall efficiency.

To elucidate this mechanism, a comparative analysis of the relevant energy levels and redox potentials was performed, including: (i) the CB edge of $CsPbBr_3$ (ii) the one-electron reduction potential of $Ni(dmgH)_2$, and (iii) the standard potential for the $O_2/O_2^{\bullet -}$ couple. MS data reveal that $Ni(dmgH)_2$ exhibits a reduction potential of –0.59 V vs. NHE, which is sufficiently negative to drive the reduction of O_2 (–0.33 V vs. NHE) to $O_2^{\bullet -}$ **(Figure 2.2c–e)**.

Since the generation of superoxide radicals is critical for aldehyde activation, the rate-limiting step in the catalytic cycle is not photoexcitation or initial charge separation, but rather the electron transfer to O_2. Hence, tuning the conduction band position of $CsPbBr_3$ and the LUMO level of the cocatalyst is vital to optimizing photoredox efficiency.

2.8. Optimization of the photoredox reaction conditions

Further optimization of the photoredox reaction conditions was conducted in various aprotic solvents, including tetrahydrofuran (THF), acetonitrile, toluene, and 1,4-dioxane. Among these, THF was identified as the optimal solvent for the photoredox C–N bond formation. To investigate the roles of the photocatalyst, cocatalyst, light, and O_2, photoredox reactions were performed with all possible combinations (**Table 2.2**). In the absence of either the photocatalyst or light, the reaction did not proceed. Under nitrogen (N_2) conditions (without O_2), only a trace amount of product (<5%) was detected. This clearly highlights the necessity of activating molecular oxygen to superoxide radicals for the photoredox reaction. However, even without the cocatalyst, $CsPbBr_3$ QDs were able to activate molecular O_2 and achieve a 48% yield of the amide product.

2.9. Substrate scope for the C–N bond formation

The C–N coupling strategy involving derivatives of benzaldehyde and piperidine demonstrated a wide substrate scope and remarkable tolerance to diverse functional groups, leading to the formation of amides in good to excellent yields (**Table 2.2**). The reactivity of aldehyde derivatives depends on the presence of electron-donating and electron-withdrawing groups in the phenyl ring of benzaldehydes. Electron-donating groups (e.g., para-methyl, para-methoxy) and ortho-substitution lowered yields (**Table 2.3, 2a–2c**), while electron-withdrawing groups (e.g., $–NO_2$) gave higher yields (82–92%, **Table 2.3, 2e–2g**). Substituent position

Table 2.2. Optimization of photoredox C–N coupling reaction conditions.

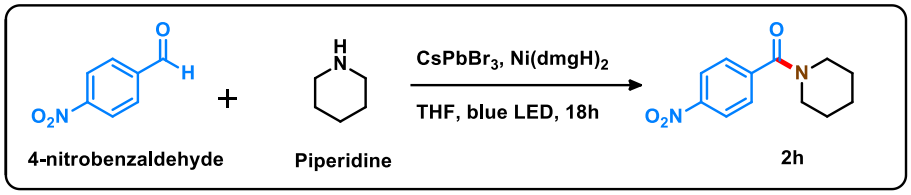

S.N.	Photocatalyst	Cocatalyst (Wt.%)	Solvent	Light	Time (h)	Yield (%)
Variation of cocatalysts						
1	$CsPbBr_3$	7 wt.% Ni-salen	Tetrahydrofuran	Blue LED	18	75
2	$CsPbBr_3$	7 wt.% $Ni(acac)_2$	Tetrahydrofuran	Blue LED	18	70
3	**$CsPbBr_3$**	**7 wt.% $Ni(dmgH)_2$**	**Tetrahydrofuran**	**Blue LED**	**18**	**92**
4	$CsPbBr_3$	7 wt.% $Ni(OAc)_2.4H_2O$	Tetrahydrofuran	Blue LED	18	49
Variation of wt.% $Ni(dmgH)_2$						
5	$CsPbBr_3$	3 wt.% $Ni(dmgH)_2$	Tetrahydrofuran	Blue LED	18	63
6	$CsPbBr_3$	5 wt.% $Ni(dmgH)_2$	Tetrahydrofuran	Blue LED	18	84
7	**$CsPbBr_3$**	**7 wt.% $Ni(dmgH)_2$**	**Tetrahydrofuran**	**Blue LED**	**18**	**92**
8	$CsPbBr_3$	9 wt.% $Ni(dmgH)_2$	Tetrahydrofuran	Blue LED	18	81
Variation of solvents						
9	$CsPbBr_3$	7 wt.% $Ni(dmgH)_2$	Acetonitrile	Blue LED	18	64
10	**$CsPbBr_3$**	**7 wt.% $Ni(dmgH)_2$**	**Tetrahydrofuran**	**Blue LED**	**18**	**92**
11	$CsPbBr_3$	7 wt.% $Ni(dmgH)_2$	1,4-Dioxane	Blue LED	18	81
12	$CsPbBr_3$	7 wt.% $Ni(dmgH)_2$	Toluene	Blue LED	18	58
Other variations in the reaction conditions						
13	-	-	Tetrahydrofuran	Blue LED	18	No Reaction
14	-	7 wt.% $Ni(dmgH)_2$	Tetrahydrofuran	Blue LED	18	No Reaction
15	$CsPbBr_3$	-	Tetrahydrofuran	Blue LED	18	48
16	$CsPbBr_3$	7 wt.% $Ni(dmgH)_2$	Tetrahydrofuran	Dark	18	5%

Reaction conditions: 10 mg catalysts, 0.5 mmol 4-nitrobenzaldehyde, and 1.0 mmol piperidine in 3.0 mL solvent, under air atmosphere. The mixture was irradiated with a 15 W blue LED at 35 ± 3 °C for 18 hours. After completion, the photocatalyst was recovered by centrifugation at 15,000 rpm for 10 minutes. The resulting product was purified through silica gel column chromatography using varying ratios of ethyl acetate and hexane as the eluent. Product identity and purity were confirmed by ^{1}H and ^{13}C NMR spectroscopy, and the isolated yield was recorded.

(ortho/meta/para) also influenced yields (**Table 2.3, 2e–2g**). 4-Bromobenzaldehyde showed a good yield (90%, **Table 2.3, 2d**). Using morpholine slightly lowered yields compared to piperidine (**Table 2.3, 2h–2j**).

Pyrrolidine reacted with various substituted benzaldehydes to yield diverse amides (**Table 2.3, 2k–n**), following trends similar to piperidine but with slightly lower yields (74–89%). The reduced efficiency arises from the higher ring strain in the five-membered pyrrolidinium amine radical intermediate compared to the more stable six-membered piperidinium radical, which destabilizes the reaction pathway and lowers the overall yield. Even ortho-hydroxyl benzaldehyde gave 56% yield (**Table 2.3, 2o**), and terephthaldehyde gave 69% (**Table 2.3, 2p**). Heterocyclic aromatic aldehydes like thiophene-2- and pyridine-2-carbaldehyde gave >80% yields (**Table 2.3, 2q–r**). The different amines also formed amides in moderate to high yields. Structural variation among similar amines had minimal impact; morpholine and pyrrolidine gave yields comparable to piperidine (**Table 2.3, 2a, 2i, 2k**), though 2-oxazolidinone gave a lower yield (**Table 2.3, 2s**).

Interestingly, aniline derivatives of pyridine and quinoline (2-aminopyridine, 2-(2-pyridyl)ethylamine, 7-aminoquinoline) produced high amide yields with benzaldehyde (**Table 2.3, 2t–2v**). In contrast, aniline produced inseparable product mixtures. Even benzylamine gave 72% yield with benzaldehyde (**Table 2.3, 2w**). However, the reaction of the aliphatic aldehyde (octanal) with benzylamine produced 55% of the amide as the major product along with 6% of the imine via the hydrogen atom transfer pathway (Table 2.3, 2x).[46]

2.10. Cocatalyst effects on ultrafast dynamics in $CsPbBr_3$ QDs

Femtosecond transient absorption spectroscopy (TAS) was employed to study the effect of $[Ni(dmgH)_2]$ on carrier relaxation dynamics in $CsPbBr_3$ QDs (**Figure 2.4**). Excitation at 370

nm generated charge carriers and trap states.[34,35] TAS of $CsPbBr_3$ (**Figure 2.4a–g**) showed: (i) a strong photobleach at 518 nm (PB1); (ii) a weaker bleach at 390–450 nm (PB2); (iii) broad excited-state absorption (ESA1, 410–510 nm); and (iv) a short-lived ESA2 (530–560 nm) decaying within 800 fs. ESA2, attributed to hot electron intra-band relaxation, blue-shifts as the energy gap widens, overlapping with and intensifying ESA1. In 7% [Ni]-$CsPbBr_3$ (**Figure 2.4h–n**), similar PB and ESA features (PB3, PB4, ESA3) were observed, though ESA2 was absent. ESA3 appeared at 510 nm, and PB3 red-shifted to 526 nm (**Figure 2.4h–n**). Despite spectral similarities, different temporal dynamics suggest the same states are involved but form at different rates.

Table 2.3. Photocatalytic C–N bond formation in the presence of visible light using 7% [Ni]-$CsPbBr_3$ photocatalyst.

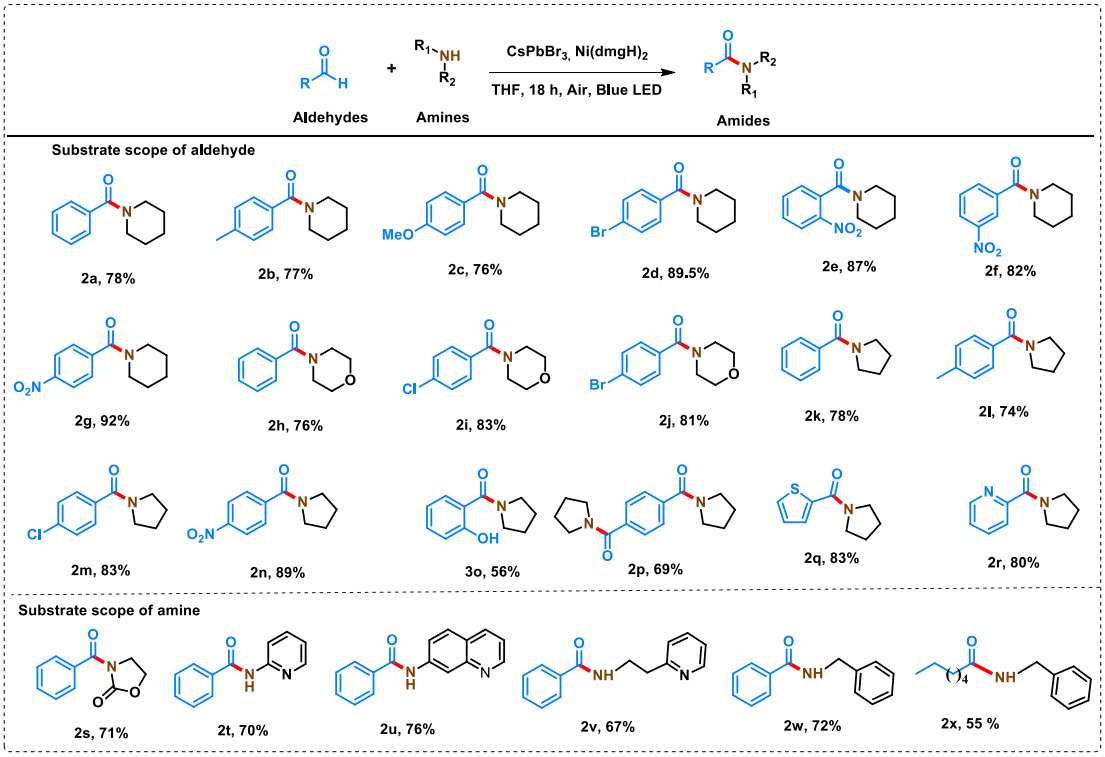

Reaction conditions: Reaction conditions: Aldehyde (0.5 mmol), amine (1.0 mmol), 7 wt% [Ni]-$CsPbBr_3$ (10 mg), THF (2.5 mL), 15 W blue LED, air atmosphere, 35 ± 3 °C, 18 h. For compound 3r, aldehyde (0.5 mmol) and pyrrolidine (2.0 mmol) were used. *All yields refer to isolated products, characterized by ^{1}H and ^{13}C NMR spectroscopy **(Table 2.4)**.

Decay dynamics were extracted by fitting kinetic traces with multi-exponential functions. The 400 nm trace corresponds to ground-state bleach to higher-energy states (**Figure 2.5a(1)**), while the 550 nm trace reflects ground-state bleach recovery, aligning with the lowest-energy band in the steady-state spectrum. Negative signals in TA may arise from ground-state bleach or stimulated emission. Hot electrons undergo intra-band relaxation, with ESA2 rising and decaying within 800 fs. However, the persistent 390–430 nm negative band, visible up to 2 ns, suggests it is not solely due to hot-electron stimulated emission, which would coincide with ESA2. In 7% [Ni]-$CsPbBr_3$, this negative band persists, while ESA2 is absent, supporting ultrafast electron transfer to the cocatalyst. Therefore, the high-energy negative band is attributed to ground-state bleach, not stimulated emission.

Kinetic traces at 500 nm show faster rise and decay for $CsPbBr_3$ compared to 7% [Ni]-$CsPbBr_3$ (**Figure 2.5a(2)**), with rise times of 98 ± 5 ps and 41 ± 2 ps, respectively. Bleach recovery at 550 nm is faster for 7% [Ni]-$CsPbBr_3$ (**Figure 2.5a(3)**), consistent with 400 nm traces. Lifetimes at 550 nm decrease from 60 ± 8 ps and 817 ± 165 ps ($CsPbBr_3$) to 31 ± 3 ps and 293 ± 32 ps (7% [Ni]-$CsPbBr_3$). Similar trends were observed at 650 nm (**Figure 2.5a(4)**). Decay-associated spectra (DAS) identified three ultrafast components: 0.8 ± 0.01 ps, 60 ± 7 ps, and 758 ± 89 ps for $CsPbBr_3$; and 1 ± 0.01 ps, 39 ± 3 ps, and 530 ± 43 ps for 7% [Ni]-$CsPbBr_3$ (**Figure 2.5b–c**).[47]

In addition to three ultrafast components, a long-lived component linked to charge recombination was observed, persisting beyond the measurement window (**Figure 2.5e–f**). The 0.8 ± 0.0 ps DAS shows a strong ESA2 band at 533 nm. At 60 ± 7 ps, a strong ESA1 band appears, which intensifies further at 760 ps, consistent with ESA1 buildup before decay. The long-lived DAS shows a positive band at 506 nm, associated with overlapping ESA1 and

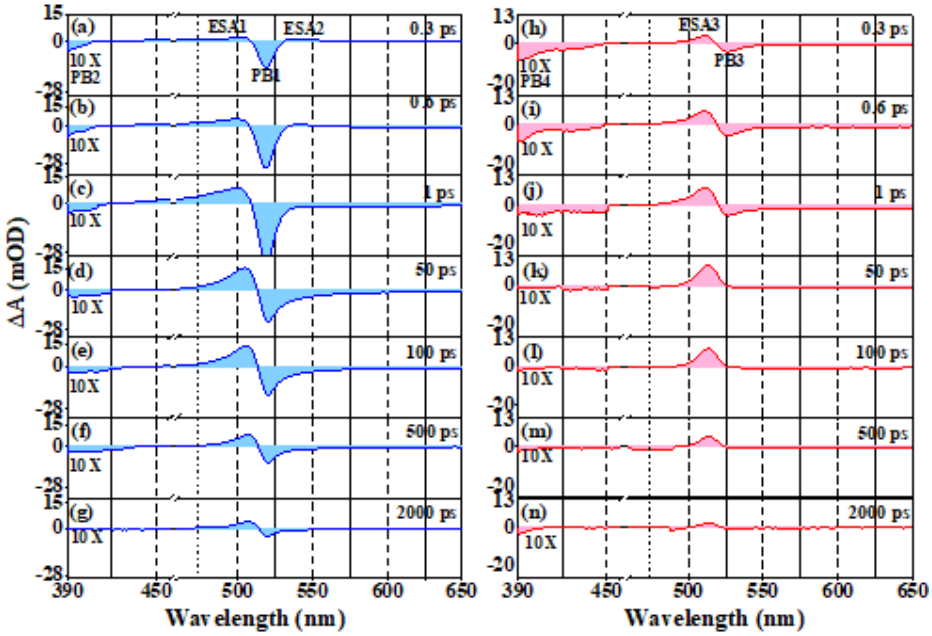

Figure 2.4. Transient absorption (TA) spectra were recorded at various pump-probe delay times for $CsPbBr_3$ (a–g) and 7% [Ni]-$CsPbBr_3$ (h–n). The spectral region between ~390 nm and 450 nm was amplified tenfold to enhance clarity. Each spectrum is labeled with its corresponding delay time. PB indicates photo-bleaching, while ESA refers to excited-state absorption.

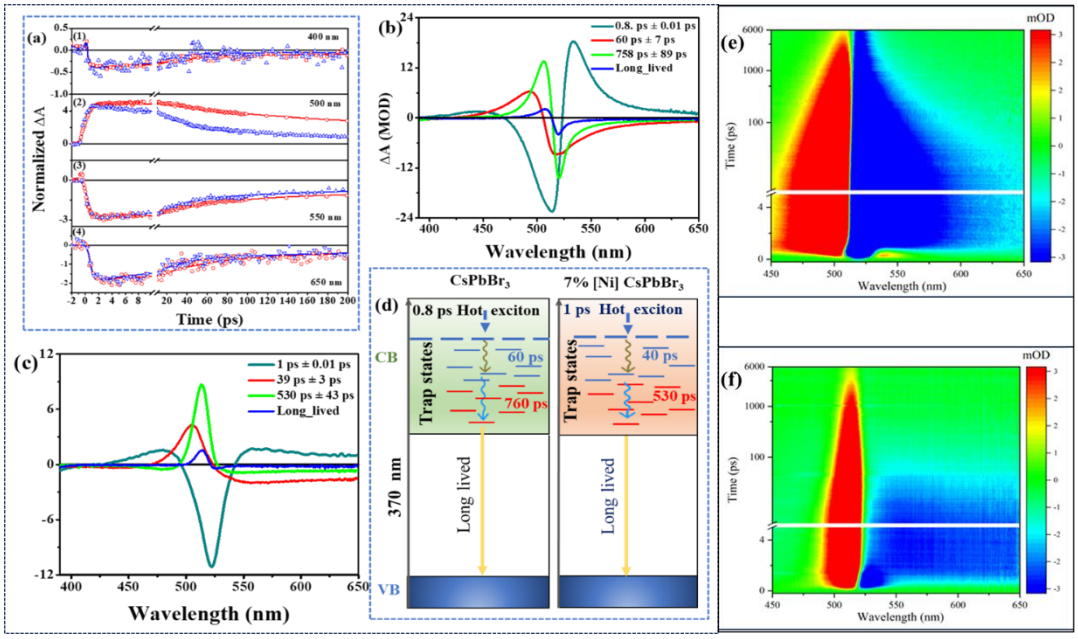

Figure 2.5. (a) Kinetic profiles measured at (1) 400 nm, (2) 500 nm, (3) 550 nm, and (4) 650 nm for $CsPbBr_3$ (red) and 7% [Ni]-$CsPbBr_3$ (blue), with solid lines representing fitted curves. (b) Decay-associated spectra (DAS) of $CsPbBr_3$ and (c) 7% [Ni]-$CsPbBr_3$. (d) Schematic representation illustrating charge carrier generation and relaxation processes in $CsPbBr_3$ and 7% [Ni]-$CsPbBr_3$. (e) TA spectra of $CsPbBr_3$ and (f) TA spectra of 7% [Ni]-$CsPbBr_3$.

PB1 features (**Figure 2.4**).[48,49] PB1 corresponds to ground-state depopulation, matching the lowest-energy steady-state absorption of the $CsPbBr_3$. The 0.8 ps rise in PB1 after 370 nm excitation reflects intra-band relaxation of high-energy excitons to the band edge.

The incorporation of $[Ni(dmgH)_2]$ into $CsPbBr_3$ leads to accelerated dynamics in the transient absorption spectra (TAS) **(Figure 2.5d)**. This faster decay is attributed to an enhanced depopulation of excited states, driven by charge migration from $CsPbBr_3$ to the $[Ni(dmgH)_2]$ complex. As a result, the average lifetime decreases in 7% [Ni]-$CsPbBr_3$, indicating the formation of trap states within the $CsPbBr_3$ matrix. Previous studies have similarly reported that the exciton bleach observed on the picosecond to nanosecond timescale serves as a signature of electron trapping in $CsPbBr_3$.[48,50,51]

Electrochemical data further support light-induced charge transfer from $CsPbBr_3$ to $[Ni(dmgH)_2]$ (**Figure 2.2i and Figure 2.3a)**. Transient absorption measurements were employed to estimate the charge transfer rate. The cocatalyst influences the lifetimes associated with exciton formation and thermal relaxation. Since the inverse of a lifetime corresponds to the rate constant of the respective process, comparing rate constants between pristine and $[Ni(dmgH)_2]$-modified $CsPbBr_3$ allows estimation of electron transfer kinetics. The trap state formation time decreases from 60 ± 8 ps in $CsPbBr_3$ to 31 ± 3 ps in 7% [Ni]-$CsPbBr_3$, corresponding to an electron transfer rate constant (k_{et}) of 1.6×10^{10} s^{-1}. This value aligns with rates typically reported for semiconductor–metal systems, where electrons have relaxed to the conduction band minimum.[51,52]

The [Ni $(dmgH)_2$] loading on $CsPbBr_3$ accelerates TAS kinetics (**Figure 2.5d**), due to faster depopulation of excited states via charge transfer to the cocatalyst. This is evidenced by reduced lifetimes in 7% [Ni]-$CsPbBr_3$, indicating trap-state formation. Prior studies have

shown that exciton bleach decay on ps–ns timescales signals electron trapping.[48-51] Electrochemical data (**Figures 2.2i, 2.3a**) confirm light-induced charge transfer from $CsPbBr_3$ to $[Ni(dmgH)_2]$. TA-derived lifetimes reflect altered exciton dynamics; the inverse lifetime gives the process rate. Trap formation time drops from 60 ± 8 ps ($CsPbBr_3$) to 31 ± 3 ps (7% [Ni]-$CsPbBr_3$), yielding an electron transfer rate constant of $k_{et} = 1.6 \times 10^{10}$ s^{-1}, consistent with rates in other semiconductor–metal systems.[51,52]

2.11. Reaction mechanism

The reaction between 4-nitrobenzaldehyde and piperidine under an inert atmosphere resulted in less than 5% product formation, underscoring the crucial role of oxygen. Additionally, introducing electron and hole scavengers ($AgNO_3$ and TEA) into the reaction mixture led to a significant decrease in product yield, indicating the involvement of free-radical pathways (**Figure 2.7a**). When para-benzoquinone, a superoxide radical scavenger, was added, the product yield dropped sharply to only 10% (**Figure 2.7a**). In the presence of $Ni(dmgH)_2$,

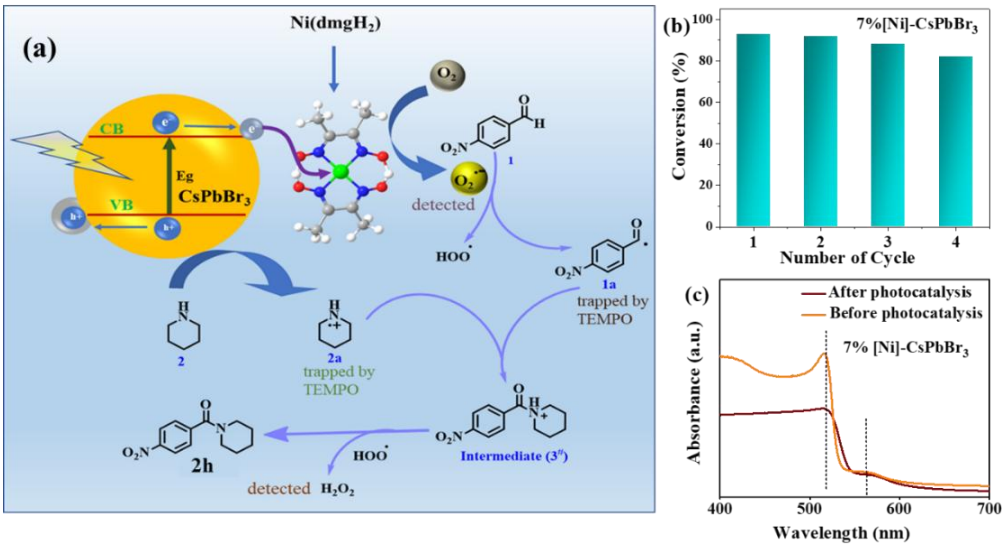

Figure 2.6. (a) Proposed mechanism of C–N bond formation under visible light. (b) Photocatalytic recyclability test for amide bond formation. (c) UV-vis spectra confirmed that the absorption peak did not change after 4 times recycling of 7%[Ni]-$CsPbBr_3$.

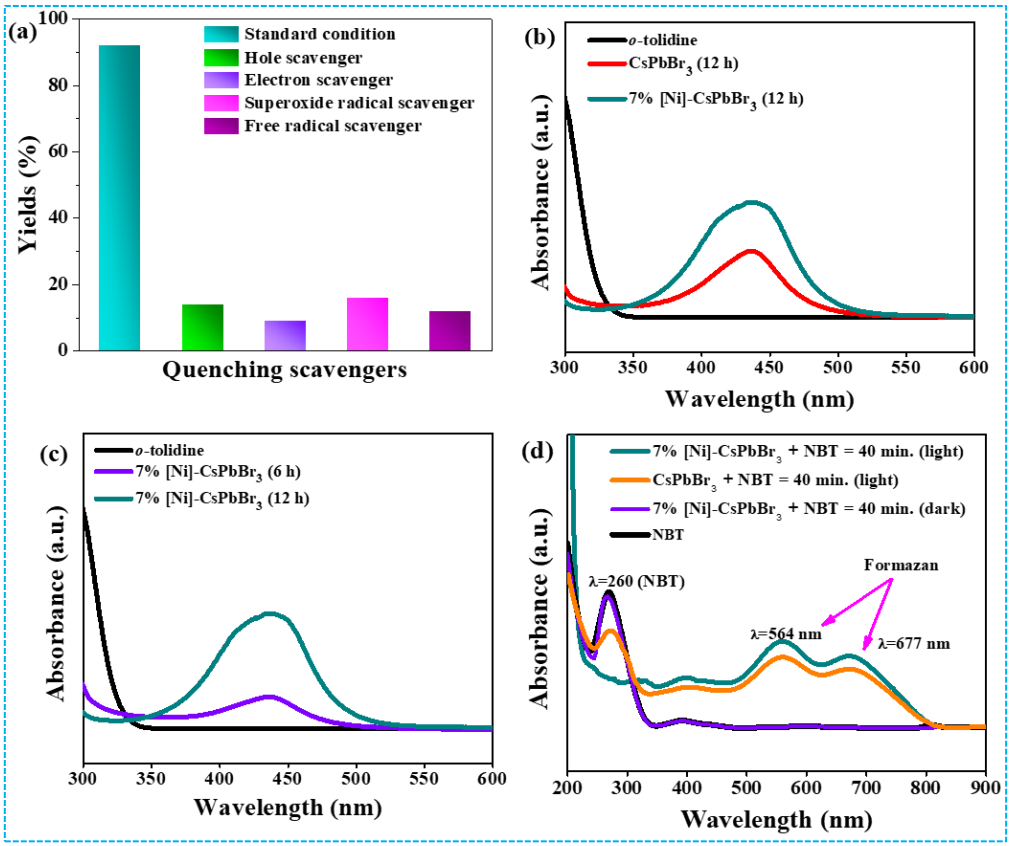

Figure 2.7. (a) Quenching experiments with different scavengers—triethylamine (hole scavenger), $AgNO_3$ (electron scavenger), p-benzoquinone (superoxide radical scavenger), and TEMPO (radical trapping agent), to identify the reactive species involved in the photocatalytic process. (b) Detection of superoxide radicals generated via dioxygen reduction during photocatalysis.

H_2O_2 detection: After the photoredox reaction, the catalyst was separated via centrifugation. Further, photoredox reaction-generated H_2O_2 from the reaction mixture was extracted into 2 mL water. Subsequently, 10 µL *o*-tolidine solution (1 wt.% tolidine in 0.1 M HCl) was added to the H_2O_2-containing solution, and UV-visible spectra were recorded. The oxidation of *o*-tolidine by photogenerated H_2O_2 resulted in a yellow-colored compound (with a maximum absorption at 436 nm). (c) Analysis of H_2O_2 formation resulting from photoredox reactions involving $CsPbBr_3$ and 7% [Ni]-$CsPbBr_3$. (d) Time-dependent detection of H_2O_2 produced during the photoredox reaction with 7% [Ni]-$CsPbBr_3$.

Superoxide radical detection: The detection of photogenerated $O_2^{\bullet-}$ by 7% [Ni]-$CsPbBr_3$ was performed using p-Nitro-blue tetrazolium chloride (NBT) as the indicator. In the presence of $O_2^{\bullet-}$, NBT undergoes reduction to form blue formazan with λ_{max} values of 564 and 677 nm. Two absorption peaks were observed for 7% [Ni]-$CsPbBr_3$ + NBT after 40 minutes of light exposure. These results conclusively demonstrate the ability of 7% [Ni]-$CsPbBr_3$ to generate $O_2^{\bullet-}$ at light, thereby confirming its role in driving the photocatalytic amide C–N coupling reaction.

electron transfer from the CB of $CsPbBr_3$ to the cocatalyst is accelerated, enabling the

subsequent reduction of surface-bound O_2 and generation of superoxide radicals. Based on these observations, we propose a mechanism for the photo-induced amide formation (**Figure 2.6a**). Upon visible-light irradiation, [Ni]-$CsPbBr_3$ undergoes photoexcitation, promoting an electron from the VB to the CB. The photogenerated electron is then transferred via the cocatalyst to atmospheric oxygen, forming a superoxide radical ($O_2^{\bullet-}$). Simultaneously, the hole (h^+) in the VB oxidises the amine (**2**), generating an amine radical cation (**2a**). The superoxide radical abstracts a hydrogen atom from 4-nitrobenzaldehyde to generate an acyl radical intermediate (**1a**) and a hydroperoxyl radical ($^{\bullet}OOH$). Notably, the intermediates 1a and 2a were successfully trapped using TEMPO and characterized by NMR spectroscopy and mass spectrometry. The radical coupling of **1a** and **2a** produces a cationic species ($3^{\#}$), which is further deprotonated by $^{\bullet}OOH$ to yield the final amide product (**2h**),[53,54] with H_2O_2 formed as a byproduct. The formation of H_2O_2 was also experimentally confirmed.[60,61] Further, the catalytic recyclability test was performed four times with minimum loss of activity (**Figure 2.6b**). The UV-visible spectrum of the recovered catalyst remained unchanged (**Figure 2.6c**). The enhanced efficiency of O_2 reduction by 7% [Ni]-$CsPbBr_3$ compared to pristine $CsPbBr_3$ was confirmed (**Figure 2.7b**). Additionally, a continuous increase in H_2O_2 concentration was observed with longer reaction times (**Figure 2.7c**), further demonstrating that 7% [Ni]-$CsPbBr_3$ is more effective at activating molecular oxygen than unmodified $CsPbBr_3$. The presence of $O_2^{\bullet-}$ was also detected by UV-visible spectroscopy (**Figure 2.7d**).[62,63] Notably, a higher generation of $O_2^{\bullet-}$ was observed for 7% [Ni]-$CsPbBr_3$ compared to the pristine QDs. Thus, in this study, we successfully detected key reaction intermediates (**1a** and **2a**) by mass spectrometry and NMR spectroscopy, along with active radical species ($O_2^{\bullet-}$) and H_2O_2 by

UV-visible spectroscopy. Based on these results and previous literature, the formation of $^{\bullet}OOH$ radicals and the intermediate **3**$^{\#}$ has been proposed to complete the catalytic cycle.[60-63]

2.12. Conclusion

In conclusion, we have demonstrated the potential of $CsPbBr_3$ QDs for the photoredox C–N coupling reaction. The introduction of a cocatalyst improved the photoredox process, and the best catalytic activity was obtained with $Ni(dmgH)_2$ because of the suitable band alignment. $Ni(dmgH)_2$ enhances photogenerated charge transfer dynamics of $CsPbBr_3$ QDs, leading to the best activity. Notably, 7% [Ni]-$CsPbBr_3$ produced the best photoredox activity, forming amide with 92% yield. Ultrafast TA measurements confirmed efficient electron transfer from $CsPbBr_3$ to $Ni(dmgH)_2$, with the rate constant of $k_{et} = 1.6\times10^{10}\ s^{-1}$. The trap states decayed significantly faster, thereby enhancing the photocatalytic activities. Importantly, the optimized reaction conditions avoid the use of external oxidants (e.g., persulfates, ceric salts, or chemical oxidants), harsh environments, ligands, additives, and toxic solvents or bases. This study has shown the potential of photoredox reactions using semiconductor QDs for the synthesis of valuable compounds.

Table 2.4: Characterization of the products by ^{1}H NMR and ^{13}C NMR spectroscopy[7-10]

2a: phenyl(piperidin-1-yl) methanone 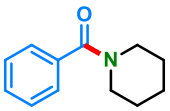	^{1}H NMR (500 MHz, $CDCl_3$) δ: 7.40 (m, 5H), 3.73 (dd, 2H), 3.35 (dd, 2H), 1.68 (m, 4H), 1.49 (m, 2H). ^{13}C NMR (125 MHz, $CDCl_3$) δ: 170.44, 136.41, 129.38, 128.39, 126.81, 48.77, 43.18, 26.04, 25.24, 24.58. **Yield: 78%, 74 mg and 0.39 mmol**
2b: (4-methylphenyl)(piperidin-1-yl) methanone[7] 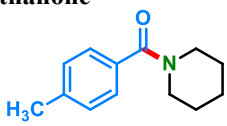	^{1}H NMR (500 MHz, $CDCl_3$) δ: 7.31 (d, J = 8.0 Hz, 2H), 7.20 (d, J = 7.8 Hz, 2H), 3.71 (m, 2H), 3.37 (m, 2H), 2.38 (s, 3H), 1.61 (m, 6H). ^{13}C NMR (125 MHz, $CDCl_3$) δ: 170.58, 139.44, 133.50, 128.98, 126.93, 48.93, 43.25, 29.69, 24.63, 21.35. **Yield: 77%, 78 mg and 0.38 mmol**

2c: (4-methoxyphenyl)(piperidin-1-yl)methanone[7] 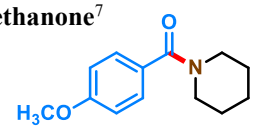	^{1}H NMR (500 MHz, $CDCl_3$) δ: 7.38 (d, J = 8.7 Hz, 2H), 6.91 (d, J = 8.7 Hz, 2H), 3.83 (s, 3H), 3.57 (m, 4H), 1.64 (m, 6H). ^{13}C NMR (125 MHz, $CDCl_3$) δ: 170.30, 160.52, 128.85, 128.64, 113.63, 54.02, 24.66. **Yield: 74%, 81 mg, and 0.36 mmol**
2d: (4-bromophenyl)(piperidin-1-yl) methanone 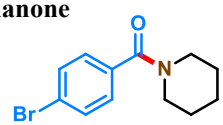	^{1}H NMR (500 MHz, $CDCl_3$) δ: 7.57 (d, *J* = 8.4 Hz, 1H), 7.31 (d, *J* = 8.4 Hz, 1H), 3.73 (dd, 2H), 3.36 (dd, 2H), 1.63 (d, 6H). ^{13}C NMR (125 MHz, $CDCl_3$) δ: 169.31, 135.26, 131.64, 128.59, 123.66, 48.84, 43.30, 26.10, 25.54, 24.52. **Yield: 89%, 103 mg, and 0.44 mmol**
2e: (2-nitrophenyl)(piperidin-1-yl) methanone 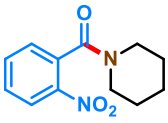	^{1}H NMR (500 MHz, $CDCl_3$) δ: 8.19 (d, J = 8.3 Hz, 1H), 7.70 (t, J = 7.5 Hz, 1H), 7.56 (t, J = 7.9 Hz, 1H), 7.39 (d, J = 7.6 Hz, 1H), 3.77 (m, 2H), 3.17 (m, 2H), 1.79–1.46 (m, 6H). ^{13}C NMR (125 MHz, $CDCl_3$) δ: 166.25, 145.25, 134.41, 133.46, 129.57, 128.00, 124.73, 47.95, 42.73, 25.81, 25.13, 24.46. **Yield: 87%, 101 mg and 0.43 mmol**
2f: (3-nitrophenyl)(piperidin-1-yl) methanone[8] 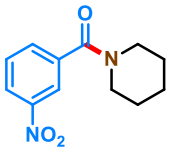	^{1}H NMR (500 MHz, $CDCl_3$) δ: 8.26 (d, J = 7.6 Hz, 2H), 7.74 (d, J = 7.3 Hz, 1H), 7.61 (t, J = 7.8 Hz, 1H), 3.73 (s, 2H), 3.34 (s, 2H), 1.63 (d, J = 77.4 Hz, 6H). ^{13}C NMR (125 MHz, $CDCl_3$) δ: 167.61, 148.05, 138.05, 132.90, 129.74, 124.23, 122.05, 48.84, 43.37, 26.52, 25.49, 24.40. **Yield: 82%, 96 mg and 0.41 mmol**
2g: (4-nitrophenyl)(piperidin-1-yl) methanone[7] 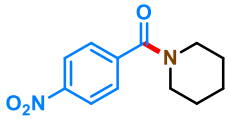	^{1}H NMR (500 MHz, $CDCl_3$) δ 8.28 (d, J = 8.7 Hz, 2H), 7.59 – 7.55 (d, 2H), 3.74 (m, 2H), 3.30 (m, 2H), 1.63 (m, 6H). ^{13}C NMR (125 MHz, CDCl3) δ 167.92, 148.22, 142.70, 127.81, 123.85, 48.66, 43.22, 26.52, 25.51, 24.40. **Yield: 92%, 107.5 mg, and 0.46 mmol**
2h: Morpholino(phenyl)methanone[9] 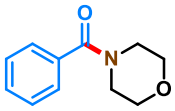	^{1}H NMR (500 MHz, $CDCl_3$) δ: 7.42 (s, 5H), 3.83–3.42 (m, 8H). ^{13}C NMR (125 MHz, $CDCl_3$) δ: 170.50, 135.28, 129.92, 128.58, 127.09, 66.90, 48.19. **Yield: 76%, 72 mg and 0.37 mmol**
2i:(4-Chlorophenyl)(morpholino)methanone 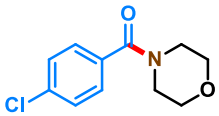	^{1}H NMR (500 MHz, $CDCl_3$) δ: 7.73 – 7.68 (m, 2H), 7.23 (d, *J* = 11.2 Hz, 2H), 4.22 – 4.10 (d, 4H), 4.01 (d, 4H). ^{13}C NMR (125 MHz, $CDCl_3$) δ: 171.46 (s), 161.93 (s), 130.21 (s), 128.32 (s), 114.81 (s), 67.92 (s), 56.36 (s). **Yield: 83%, 93 mg and 0.41 mmol**
2j: (4-bromophenyl)(morpholino) methanone[8] 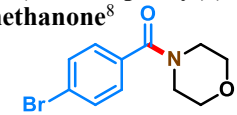	^{1}H NMR (500 MHz, $CDCl_3$) δ: 7.40 (d, J = 8.7 Hz, 2H), 6.92 (d, J = 8.7 Hz, 2H), 3.84 (d, 2H), 3.70 (d, 2H), ^{13}C NMR (125 MHz, $CDCl_3$) δ: 170.44, 160.93, 129.20, 127.33, 113.80, 66.92, 55.36.

	Yield: 81%, 108 mg and 0.40 mmol
2k: phenyl(pyrrolidine-1-yl) Methanone[7] 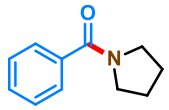	^{1}H NMR (600 MHz, CDCl3) δ: 7.49 (d, J = 6.4 Hz, 2H), 7.37 (d, J = 5.5 Hz, 3H), 3.63 (t, 2H), 3.40 (t, 2H), 1.89 (dt, 4H). ^{13}C NMR (150 MHz, $CDCl_3$) δ: 169.80, 137.10, 129.80, 128.23, 127.05, 49.62, 46.19, 26.35, 24.43. **Yield: 76%, 66 mg and 0.37 mmol**
2l: (4-methylphenyl)(pyrrolidin-1-yl) methanone[8] 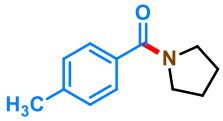	^{1}H NMR (600 MHz, $CDCl_3$) δ: 7.34 (d, *J* = 7.4 Hz, 2H), 7.11 (d, *J* = 7.4 Hz, 2H), 3.56 (t, 2H), 3.36 (t, 2H), 2.29 (s, 3H), 1.83 (m, 4H). ^{13}C NMR (150 MHz, $CDCl_3$) δ: 169.90, 139.94, 134.22, 128.82, 127.20, 49.68, 46.22, 26.40, 24.45, 21.38. **Yield: 74%, 70 mg and 0.36 mmol**
2m: (4-chlorophenyl)(piperidin-1-yl) methanone[8] 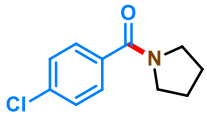	1H NMR (600 MHz, CDCl3) δ: 7.46 (d, J = 8.1 Hz, 2H), 7.37 (d, J = 8.2 Hz, 2H), 3.63 (t, 2H), 3.41 (t, 2H), 1.92 (dt, 4H). ^{13}C NMR (150 MHz, $CDCl_3$) δ: 168.64, 135.86, 135.44, 128.66, 128.52, 49.64, 46.33, 26.40, 24.40. **Yield: 83%, 86.5 mg and 0.41 mmol**
2n: (4-nitrophenyl)(piperidin-1-yl) methanone[7] 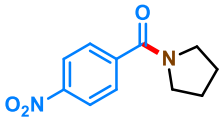	^{1}H NMR (600 MHz, CDCl3) δ: 8.25 (d, J = 8.0 Hz, 2H), 7.67 (d, J = 7.9 Hz, 2H), 3.65 (t, 2H), 3.37 (t, 2H), 1.95 (dt, 2H), 1.84 – 1.78 (m, 2H). ^{13}C NMR (150 MHz, $CDCl_3$) δ: 167.43, 148.40, 143.08, 128.14, 123.68, 49.45, 46.39, 26.35, 24.34. **Yield: 89%, 97 mg and 0.44 mmol**
2o: (2-hydroxyphenyl)(pyrrolidin-1-yl)methanones 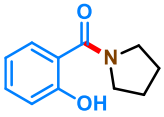	^{1}H NMR (500 MHz, $CDCl_3$) δ: 7.19 (t, *J* = 7.9 Hz, 1H), 7.11 (s, 1H), 6.95 (d, *J* = 7.6 Hz, 1H), 6.90 (dd, *J* = 8.2, 2.5 Hz, 1H), 3.64 (t, 2H), 3.42 (t, 2H), 1.91 (dt, 4H). ^{13}C NMR (126 MHz, $CDCl_3$) δ: 170.19, 157.07, 137.39, 129.31, 117.79, 117.52, 114.49, 49.68, 46.30, 26.15, 24.29. **Yield: 56%, 54 mg and 0.41 mmol**
2p: Phenylenebis(pyrrolidine-1-yl) methanone 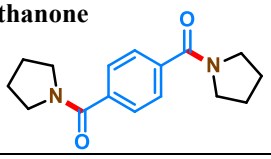	^{1}H NMR (500 MHz, $CDCl_3$) δ: 7.56 (s, 1H), 3.67 (t, 2H), 3.42 (t, 2H), 2.01 – 1.97 (m, 2H), 1.91 (d, 2H). ^{13}C NMR (125 MHz, $CDCl_3$) δ: 169.05, 138.54, 127.06, 49.54, 46.22, 26.37, 24.44. **Yield: 69%, 93 mg and 0.34 mmol**
2q: pyrrolodin-1-yl(thiophene-2-yl)methanone[10] 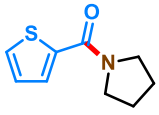	^{1}H NMR (500 MHz, $CDCl_3$) δ: 7.54 (d, *J* = 3.7 Hz, 1H), 7.48 (d, *J* = 5.0 Hz, 1H), 7.09 (m, 1H), 3.73 (m, 4H), 1.99 (m, 4H). ^{13}C NMR (125 MHz, $CDCl_3$) δ: 161.89, 139.48, 129.62, 129.57, 127.05, 48.93, 47.34, 26.72, 24.08. **Yield: 83%, 75 mg and 0.41 mmol**
2r: Pyridin-2yl(pyrrolidin-1-yl) methanone[10]	^{1}H NMR (500 MHz, $CDCl_3$) δ: 8.50 (d, 1H), 7.72 (m, 2H), 7.26 (d, 1H), 3.62 (m, 4H), 1.84 (m, 4H).

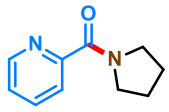	^{13}C NMR (126 MHz, $CDCl_3$) δ: 166.47, 154.42, 147.93, 136.79, 124.63, 123.70, 49.01, 46.77, 26.49, 23.96. **Yield: 80%, 70 mg, and 0.40 mmol**
2s: 3-benzoyloxazolidin-2-one 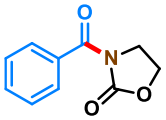	^{1}H NMR (500 MHz, $CDCl_3$) δ: 7.68 (dd, *J* = 8.2, 1.0 Hz, 2H), 7.57 (t, *J* = 7.5 Hz, 1H), 7.45 (t, *J* = 7.8 Hz, 2H), 4.49 (t, 2H), 4.18 (t, 2H). ^{13}C NMR (125 MHz, $CDCl_3$) δ: 169.82, 153.25, 132.66, 132.40, 129.09, 127.89, 62.27, 43.72. **Yield: 71%, 67 mg and 0.35 mmol**
2t: N-(pyridin-2-yl)benzamide 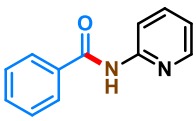	^{1}H NMR (500 MHz, $CDCl_3$) δ: 9.37 (s, 1H), 8.46 (d, *J* = 8.4 Hz, 1H), 8.23 – 8.13 (m, 1H), 7.99 (d, *J* = 7.2 Hz, 2H), 7.79 (s, 1H), 7.57 (d, *J* = 8.6 Hz, 1H), 7.52 (d, *J* = 7.8 Hz, 2H), 7.08 (s, 1H). ^{13}C NMR (125 MHz, $CDCl_3$) δ: 171.23, 166.08, 151.75, 147.50, 138.75, 134.26, 132.25, 129.97, 128.78, 127.48, 119.89, 114.57. **Yield: 70%, 69 mg and 0.35 mmol**
2u: N-(Quinolin-7-yl) benzamide 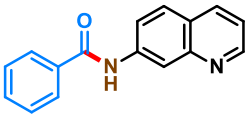	^{1}H NMR (500 MHz, $CDCl_3$) δ: 10.78 (s, 1H), 8.97 (d, *J* = 7.6 Hz, 1H), 8.87 (d, *J* = 5.8 Hz, 1H), 8.21 (dd, *J* = 8.2, 1.4 Hz, 1H), 8.12 (dd, *J* = 8.0, 1.5 Hz, 2H), 7.60 (m, 5H), 7.50 (dd, 1H). ^{13}C NMR (125 MHz, $CDCl_3$) δ: 165.49, 148.31, 138.82, 136.41, 135.21, 134.63, 131.85, 128.82, 128.03, 127.49, 127.32, 121.70, 116.58. **Yield: 76%, 94 mg and 0.38 mmol**
2v: N-(2-(pyridin-2-yl)ethyl)benzamide 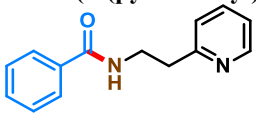	^{1}H NMR (500 MHz, $CDCl_3$) δ: 8.54 (d, *J* = 4.8 Hz, 1H), 7.78 (d, *J* = 7.1 Hz, 2H), 7.63 (t, *J* = 7.7 Hz, 2H), 7.48 – 7.38 (m, 3H), 7.22 – 7.15 (m, 2H), 3.88 – 3.83 (m, 2H), 3.10 (t, *J* = 6.3 Hz, 2H). ^{13}C NMR (125 MHz, $CDCl_3$) δ: 167.41, 159.74, 149.04, 136.92, 134.70, 131.27, 128.47, 123.64, 121.73, 39.30, 36.63. **Yield: 67%, 76 mg and 0.34 mmol**
2w: N-benzylbenzamide[11] 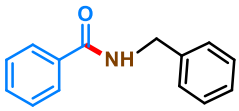	^{1}H NMR (500 MHz, $CDCl_3$) δ: 7.83 – 7.80 (d, 2H), 7.51 (d, J = 7.9 Hz, 1H), 7.44 (d, 2H), 7.37 (d, 4H), 7.33 (m, 1H), 6.55 (d, 1H), 4.67 (s, 2H). ^{13}C NMR (125 MHz, $CDCl_3$) δ: 167.35, 138.15, 134.43, 131.57, 128.80, 128.60, 127.93, 127.63, 126.99, 44.16 **Yield: 72%, 75 mg and 0.35 mmol**
2x: N-benzyloctanamide 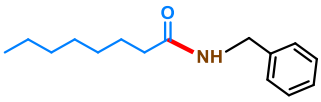	^{1}H NMR (500 MHz, $CDCl_3$) δ: 7.38 – 7.33 (d, 2H), 7.29 (t, J = 6.5 Hz, 3H), 6.00 – 5.86 (s, 1H), 4.47 (s, 2H), 3.05 (t, 2H), 2.26 – 2.20 (m, 2H), 1.72 – 1.65 (m, 2H), 1.35 – 1.28 (m, 6H), 0.91 (t, 3H). ^{13}CMR (125 MHz, $CDCl_3$) δ: 173.05, 128.69, 127.82, 127.47, 106.56, 43.58, 39.15, 36.77, 31.49, 29.69, 25.46, 22.39, 13.93. **Yield: 55%, 64 mg and 0.27 mmol**

2.13. ^{1}H NMR and ^{13}C NMR spectra of the product.

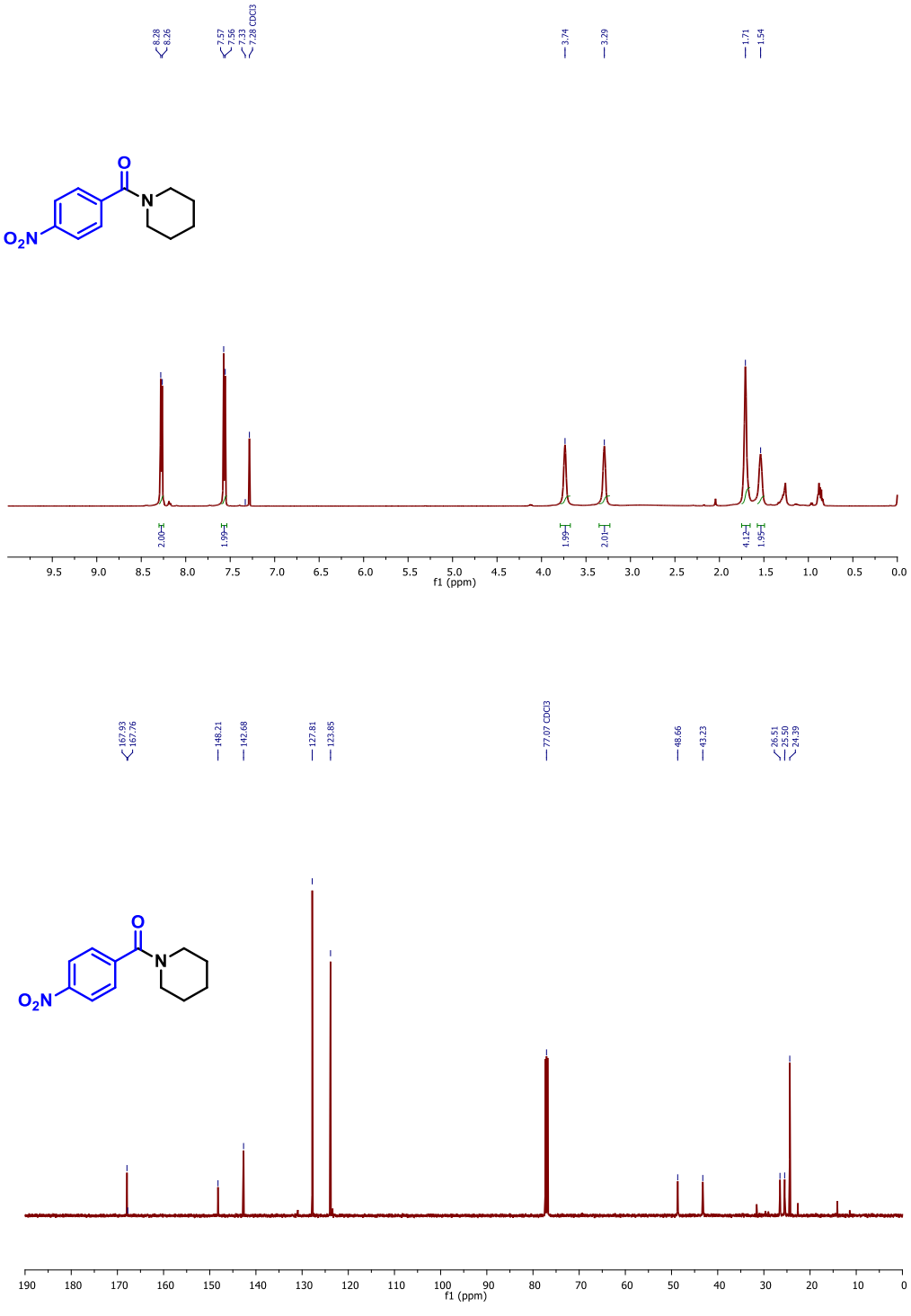

Figure 2.8. ^{1}H NMR and ^{13}C NMR spectra of the compound **2h**.

2.14. References

1. C. Russo, F. Brunelli, G. C. Tron and M. Giustiniano, *J. Org. Chem.*, 2023, **88**, 6284–6293.
2. G. E. M. Crisenza and P. Melchiorre, *Nat. Commun.*, 2020, **11**, 803.
3. H. Huang, B. Pradhan, J. Hofkens, M. B. J. Roeffaers, and J. A. Steele, *ACS Energy Lett.*, 2020, **5**, 1107–1123.
4. D. Sun, Y. Chen, X. Yu, Y. Yin and G. Tian, *Chem. Eng. J.*, 2023, **462**, 142084.
5. P. Sha, L. Huang, J. Zhao, Z. Wu, Q. Wang, L. Li, D. Bu and S. Huang, *ACS Catal.*, 2023, **13**, 10474–10486.
6. A. Wang, M. Du, J. Ni, D. Liu, Y. Pan, X. Liang, D. Liu, J. Ma, J. Wang and W. Wang, *Nat. Commun.*, 2023, **14**, 6733.
7. Y. Zheng, Y. Chen, B. Gao, B. Lin, and X. Wang, *Adv. Funct. Mater.*, 2020, **30**, 2002021.
8. A. Indra, R. Beltrán-Suito, M. Müller, R. P. Sivasankaran, M. Schwarze, A. Acharjya, B. Pradhan, J. Hofkens, A. Brückner, A. Thomas, P. W. Menezes and M. Driess, *ChemSusChem*, 2021, **14**, 306–312.
9. A. Indra, P.W. Menezes, M. Schwarze, and M. Driess, *New J. Chem.*, 2014. **38,** 1942-1945.
10. A. Indra, P. W. Menezes, K. Kailasam, D. Hollmann, M. Schröder, A. Thomas, A. Brückner and M. Driess, *Chem. Commun.*, 2016, **52**, 104–107.
11. S. Alemdar, A. Basak, and O. Metin, *ACS Appl. Mater. Interfaces*, *ACS Appl. Mater. Interfaces* 2023, **15**, 48096-48109.
12. A. P. Deshmukh, K. Patil, S. Ogale, and T. Bhave, *ACS Appl. Electron. Mater.*, 2023, **5**, 1536–1545.
13. H. Kasap, C. A. Caputo, B. C. M. Martindale, R. Godin, V. W. H. Lau, B. V. Lotsch, J. R. Durrant, and E. Reisner, *J. Am. Chem. Soc.*, 2016, **138**, 9183–9192.
14. H. Jiang, M. Liu, X. Lian, M. Zhu, and F. Zhang, *Angew. Chem. Int. Edt.* 2024, **136**, e202318850.
15. I. Rosa-Pardo, C. Casadevall, L. Schmidt, M. Claros, R. E. Galian, J. Lloret-Fillol and J. P. Prieto, *Chem. Commun.*, 2020, **56**, 5026–5029.
16. Q. Fan, H. Zhang, D. Liu, C. Yan, H. Zhu, Z. Xie and Z. Le, *J. Org. Chem.*, 2023, **88**, 7391–7400.
17. Lee, Jinsun, A. Kumar and H. Tuysuz, *Angew. Chem. Int. Ed.* 2024, 202404496.
18. K. Mishra, D. Guyon, J. San Martin and Y. Yan, *J. Am. Chem. Soc.*, 2023, **145**, 17242–17252.
19. Y. Dong, Y. Feng, Z. Li, H. Zhou, H. Lv, H. and G. Y. Yang, *ACS Catal.* 2023, **13**, 14346–14355.
20. X. Zhu, Y. Lin, Y. Sun, M. C. Beard and Y. Yan, *J. Am. Chem. Soc.*, 2019, **141**, 733–738.

21. X. Zhu, Y. Lin, J. San Martin, Y. Sun, D. Zhu and Y. Yan, *Nat. Commun.*, 2019, **10**, 2843.
22. K. Chen, X. Deng and G. Dodekatos, *J. Am. Chem. Soc.* 2017**, 139**, 12267–12273.
23. Y. Yuan, H. Zhu, K. H. Kimball, T. Cai, W. Shi, Z. Wei, H. Yang, Y. Candler, P. Wang, J. He and O. Chen, *Angew. Chem. Int. Ed*, 2020, **59,** 22563–22569.
24. J. S. Martin, X. Zeng, X. Chen, C. Miller, C. Han, Y. Lin, N. Yamamoto, X. Wang, S. Yazdi, Y. Yan, M. C. Beard and Y. Yan, , *J. Am. Chem. Soc.* 2021, **143,** 11361–11369.
25. W. Wu, Y.C. Wong, Z. K. Tan, and J. Wu, *Catal. Sci. & Technol.,* 2018, **8**, 4257-4263.
26. L. Xu, S. Z. Zhang, W. Li and Z. H. Zhang, *Chem. Eur. J.*, 2021, **27**, 5483–5491.
27. L. Deng, L. Chen, L. Zhu, Y. Li, J. Ou-Yang, S. Wu, P. Chen, S. Shen, J. Guo, Y. Zhou, C. T. Au and S. F. Yin, *Chem. Eng. Sci.*, 2022, **261**, 117960.
28. B. Goel, V. Vyas, N. Tripathi, A. K. Singh, P. W. Menezes, A. Indra, and S.K. Jain, *ChemCatChem*, 2020, **12**, 5743-5749.
29. V. Vyas, V. Kumar and A. Indra, *Chem. Commun.*, 2024, **60**, 2544–2547.
30. O. G. Mountanea, D. Psathopoulou, C. Mantzourani, M. G. Kokotou, E. A. Routsi, D. Tzeli, C. G. Kokotos and G. Kokotos, *Chem. Eur. J.* 2023*,* **29***, 2300556.*
31. N. Martín and F. G. Cirujano, *Catal. Commun.*, 2022, **164**, 106420.
32. A. Hassan Tolba, M. Krupička, J. Chudoba and R. Cibulka, *Org. Lett.*, 2021, **23**, 6825–6830.
33. Y. C. Pu, Y. H. Chuang, M. W. Zheng, Y. J. Chang and S. H. Liu, *J. Environ. Chem. Eng.*, 2023, **11**, 109103.
34. H. Wang, W. Lu, P. Xu, J. Luo, K. Yao, J. Zhang, X. Wei, S. Peng, H. Cheng, H. Hu and K. Sun, *ACS Sustain. Chem. Eng.*, 2023, **11**, 5963–5972.
35. J. Ding, X. Deng, J. Fan, Y. Wang, Z. Li and Q. Liang, *Inorg. Chem.*, 2023, **62**, 16493–16502.
36. X. Deng, Q. Liang, J. Fan, X. Yan, H. Si, H. Huang, Z. Li and Z. Kang, *Chem. Eng. J.*, 2023, **475**, 146385.
37. F. Xu, K. Meng, B. Cheng, S. Wang, J. Xu and J. Yu, *Nat. Commun.*, 2020, **11**, 14613.
38. S. Liu, F. Li, T. Li and W. Cao, *J. Colloid Interface Sci.*, 2023, **642**, 100–111.
39. Z. Zhang, L. Li, Y. Jiang and J. Xu, *Inorg. Chem.*, 2022, **61**, 3351–3360.
40. J. Ma, W. Meng, L. Zhang, F. Li and T. Li, *RSC Adv.*, 2021, **11**, 5035–5043.
41. Y. Zhang, L. Shi, H. Yuan, X. Sun, X. Li, L. Duan, Q. Li, Z. Huang, X. Ban and D. Zhang, *Chem. Eng. J.*, 2022, **430**, 132820.
42. Z. Chen, Y. Hu, J. Wang, Q. Shen, Y. Zhang, C. Ding, Y. Bai, G. Jiang, Z. Li and N. Gaponik, *Chem. Mater.*, 2020, **32**, 1517–1525.
43. S. Y. Ali, K. D. Reddy and A. K. Manna, *J. Phys. Chem. A*, 2019, **123**, 9166–9174.
44. Y. F. Xu, M. Z. Yang, H. Y. Chen, J. F. Liao, X. D. Wang and D. Bin Kuang, *ACS Appl. Energy Mater.*, 2018, **1**, 5083–5089.
45. W. Gong, Y. Li, Y. Yang, H. Guo and X. Niu, *J. Mater. Chem. C*, 2023, **11**, 6963–6970.

46. A. J. McMillan, M. Sieńkowska, P. Di Lorenzo, G. K. Gransbury, N. F. Chilton, M. Salamone, A. Ruffoni, M. Bietti and D. Leonori, *Angew. Chem. Int. Ed.* 2021, **133**, 7208–7215.
47. I. H. M. Van Stokkum, D. S. Larsen and R. Van Grondelle, *Biochim. Biophys. Acta - Bioenerg.*, 2004, **1657**, 82–104.
48. K. Wu, G. Liang, Q. Shang, Y. Ren, D. Kong and T. Lian, *J. Am. Chem. Soc.*, 2015, **137**, 12792–12795.
49. F. Deschler, M. Price, S. Pathak, L. E. Klintberg, D. D. Jarausch, R. Higler, S. Hüttner, T. Leijtens, S. D. Stranks, H. J. Snaith, M. Atatüre, R. T. Phillips and R. H. Friend, *J. Phys. Chem. Lett.*, 2014, **5**, 1421–1426.
50. C. Harris and P. V. Kamat, *ACS Nano*, 2010, **4**, 7321–7330.
51. K. Wu, H. Zhu, Z. Liu, W. Rodr and T. Lian, *J. Am. Chem. Soc.*, 2012, 10337–10340.
52. G. Nanoparticles, W. Virginia and U. States, *J. Phys. Chem. Lett.*, 2011, **2**, 2125–2129.
53. Z. Akrami and M. Hosseini-Sarvari, *European J. Org. Chem.*, 2022*,* 202200429.
54. A. Dey, S. Chakraborty, A. Singh, F.A. Rahimi, S. Biswas, T. Mandal, and T.K. Maji, *Angew. Chem. Int. Ed*, 2024, e202403093.
55. F. K. C. Leung, J. F. Cui, T. W. Hui, K. K. Y. Kung and M. K. Wong, *Asian J. Org. Chem.*, 2015, **4**, 533–536.
56. L. Deng, L. Chen, L. Zhu, Y. Li, J. Ou-Yang, S. Wu, P. Chen, S. Shen, J. Guo, Y. Zhou, and C.T. Au. *Chem. Eng. Sci.* 2022, **261,**117960.
57. D. Leow, *Org. Lett.,* 2014, **16,** 5812–5815.
58. A. Banerjee, Z. Ley, M.Y. Ngai, *Synthesis* **2019**, *51*, 303-333.
59. L. Wang, M. Yu, C. Wu, N. Deng, C. Wang, and X. Yao. *Adv. Syn. & Catal*., 2016, **358,** 2631-2641.
60. L. Magerusan, C. Socaci, F. Pogacean, M. C. Rosu, A. R. Biris, M. Coros, A. Turza, V. Floare-Avram, G. Katona and S. Pruneanu, *RSC Adv.*, 2016, **6**, 79497–79506.
61. A. K. Singh, D. Hollmann, M. Schwarze, C. Panda, B. Singh, P. W. Menezes and A. Indra, *Adv. Sustain. Syst.*, 2021, **5**, 2000288.
62. J. Luo, X. Wei, Y. Qiao, C. Wu, L. Li, L. Chen and Ji. Shi, *Adv. Mater*. 2023, **35**, 2210110.
63. A. K. Singh, K. Bijalwan, N. Kaushal, A. Kumari, A. Saha and A. Indra, *ACS Appl. Nano Mater*., 2023, **6,** 8036–8045.